



Central South Pacific thermocline water circulation from a high-resolution ocean model validated against satellite data: Seasonal variability and El Niño 1997–1998 influence

Elodie Martinez,^{1,2} Alexandre Ganachaud,^{3,4,5} Jerome Lefevre,^{3,4} and Keitapu Maamaatuaiahutapu¹

Received 21 March 2008; revised 12 January 2009; accepted 28 January 2009; published 13 May 2009.

[1] The oceanic circulation in French Polynesia, central South Pacific, is investigated based on a high-resolution model validated with satellite data. We focus on the upper 500 m, where ocean current variability has been barely documented due to a lack of in situ measurements. Seasonal and El Niño–Southern Oscillation 1997–1999 variability of surface and subsurface currents are characterized. In the north, the South Equatorial Current (SEC) follows a seasonal cycle with winter enhancement corresponding to trade wind strengthening. During summer, the SEC slows and the eastward South Equatorial Countercurrent (SECC) appears across the domain north of an upward Ekman pumping region related to the South Pacific Convergence Zone development in the area. Around the Marquesas Islands, a wind curl dipole is suspected to create westward and eastward (Marquesas Countercurrent, MCC) jets. The eastward Subtropical Countercurrent (STCC) is found south of 20°S. It is disturbed by eddies and broken into westward and eastward branches. During El Niño 1997–1998, due to the reversed winds in the equatorial band, the SEC weakened, while eastward countercurrents appeared. The SECC reinforced and moved northeastward in summer 1998. During La Niña 1998–1999, following the trade wind enhancement, the SEC strengthened. The countercurrents weakened or disappeared and the SECC moved southwestward in summer 1999. During both El Niño and La Niña events, the STCC eddy activity strengthened, while the MCC and associated westward jet were absent. These variations and their dynamical origins are discussed, and a coherent picture of the French Polynesian current system and its variations is proposed.

Citation: Martinez, E., A. Ganachaud, J. Lefevre, and K. Maamaatuaiahutapu (2009), Central South Pacific thermocline water circulation from a high-resolution ocean model validated against satellite data: Seasonal variability and El Niño 1997–1998 influence, *J. Geophys. Res.*, 114, C05012, doi:10.1029/2008JC004824.

1. Introduction

[2] Most South Pacific Ocean studies have been focused on its western or eastern part, leaving the central South Pacific barely documented [Kessler and Taft, 1987; Morris *et al.*, 1996; Delcroix and Picaut, 1998; Penven *et al.*, 2005; Kessler, 2006; Fiedler and Talley, 2006]. The region of interest here is that of French Polynesia ([5°–30°S] [160°–130°W]), including its five archipelagoes (Figure 1). It is influenced locally by the easterly trade winds, with some

seasonal and interannual modulations associated with displacement of the South Pacific Convergence Zone (SPCZ). Numerical experiment by Wang *et al.* [2000] suggests that French Polynesia is a region where the thermocline depth variability is mostly seasonal, except along the SPCZ where interannual variations become important. Their sensitivity experiments indicated that those seasonal variations were barely influenced by oceanic equatorial dynamics whose main impacts are north of 5°S. Rather, the region is under influence of local Ekman pumping and other unidentified South Pacific processes.

[3] Neither ocean currents nor ocean temperature variability are well described because of the lack of in situ measurements. Basin-scale studies using expendable bathythermographs (XBTs, which provide temperature down to 400–800 m along ship routes) and satellite data identified two dominant features in the French Polynesian region [Lagerloef *et al.*, 1999; Delcroix *et al.*, 2005]. From 0°S to 20°S the north limb of the South Pacific gyre flows westward as the South Equatorial Current (SEC), with stronger velocities during winter and some intermittent countercurrents during summer. South of 20°S the Subtrop-

¹Laboratoire Terre-Océan, Université de la Polynésie Française, Faaa, French Polynesia.

²Now at UMR7093, UMPC, CNRS, Villefranche-sur-Mer, France.

³Laboratoire d'Etude en Géophysique et Océanographie Spatiales, Institut de Recherche pour le Développement, Noumea, New Caledonia.

⁴Also at Observatoire Midi-Pyrénées–Physique-Chimie-Automatique, Laboratoire d'Etude en Géophysique et Océanographie Spatiales, Université Paul Sabatier, Toulouse, France.

⁵Also at Joint Institute for the Study of the Atmosphere and Ocean, Pacific Marine Environmental Laboratory, NOAA, Seattle, Washington, USA.

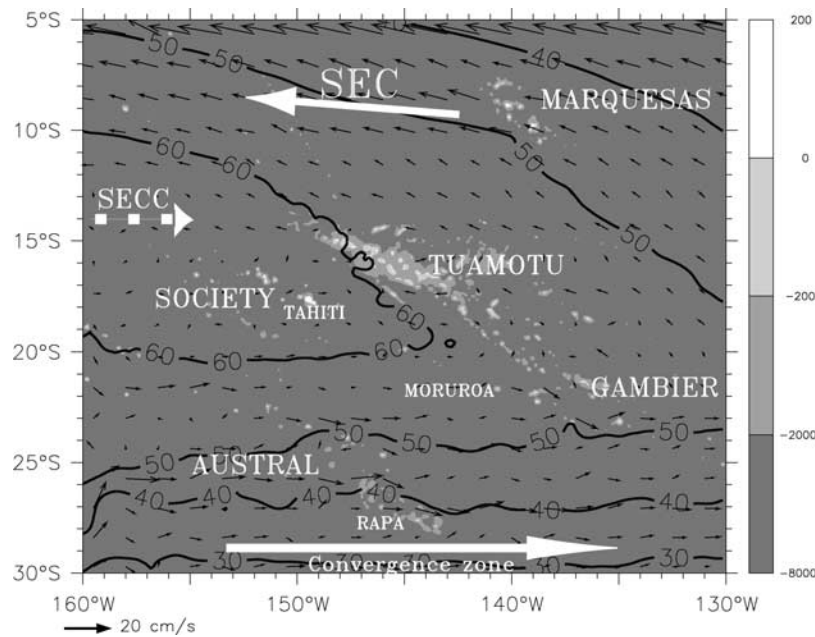


Figure 1. French Polynesian bathymetry (in meters) and main archipelagos. Overlain is the regional ocean modeling system (ROMS) mean sea surface height (SSH) (contours) and the ROMS mean geostrophic surface currents (names with the corresponding arrows are indicated), the South Equatorial Current (SEC), the oceanic convergence zone to the south, and the intermittent (dashed arrow) South Equatorial Countercurrent (SECC). Archipelago names are indicated (larger sizes), as are the islands of Tahiti, Rapa, and Moruroa.

ical Countercurrent (STCC) [Merle *et al.*, 1969] flows eastward (Figure 1), above a deeper westward flow belonging to the SEC. This eastward flow arises from the spreading of the thermocline whose deeper isopycnals slope down toward the poles (westward flow), while shallow isopycnals slope up to the surface (surface eastward flow) [Huang and Qiu, 1998]. Those currents are altered by the local wind field and by their encounter with islands and archipelagos.

[4] The first substantial work on circulation in French Polynesia was the Hawaii-to-Tahiti Shuttle Experiment (hereafter referred as the “Shuttle”) [Wyrki and Kilonsky, 1984], which provided repeated temperature and salinity measurements over the water column from April 1979 to June 1980 and allowed a description of the mean and variability of the zonal geostrophic currents and transports across 150°W from Tahiti (17°S) to Hawaii (21°N). The authors identified an intense (weak) transport in the SEC north (south) of 8°S. They also identified an intermittent eastward countercurrent between 7 and 14°S, the South Equatorial Countercurrent (SECC) that occasionally formed several branches [Eldin, 1983]. Below the SEC and near 6–7°S, the Southern Subsurface Countercurrent (SSCC) was found with two branches. Similar work was done during the “Hydropol” program, a series of biannual cruises from 1986 to 1989, between Tahiti, Rapa, the Marquesas and Moruroa (Figure 1), which enabled identification of several important features between 8°–28°S and 140°–145°W [Rancher *et al.*, 1992; Rougerie and Rancher, 1994; Rancher and Rougerie, 1995] such as a countercurrent near the Marquesas Archipelago (10°S, 140°W) named the Marquesas Countercurrent (MCC), and an area of high variability around the Gambier archipelago. South of 23°S, eastward flows were observed and were reported to feed the subtrop-

ical eastward drift that continues the southern branch of the subtropical gyre. This work also described the 1987 El Niño event with a weakening of the SEC and a strengthening of the eastward flows with the SECC and countercurrents in the northern region, and the eastward drift in the south.

[5] On the basis of geostrophic and Ekman surface currents estimated from satellite data from 1993 to 2001 (TP/ERS SSHA and ERS-1 and -2 wind data), Martinez *et al.* [2007] calculated the mean and variability of surface currents in French Polynesia, showing important seasonal and interannual variations. The present study extends their description to the subsurface currents and to higher spatial resolution. Because of the large spatial and temporal variations measured in the surface fields, the coarse distribution of hydrographic data is insufficient, and a regional ocean model is used to complement the surface satellite data. Section 2 presents the regional model. It is followed by a brief description of the mean surface properties (section 3). The seasonal variability of both surface and subsurface currents is presented in section 4, along with the El Niño 1997–98 influence (section 5). The results are summarized and discussed in section 6.

2. Numerical Model and Configuration

[6] The regional ocean modeling system (ROMS) used here was developed at UCLA, Rutgers University and IRD (<http://roms.mpl.ird.fr/>). ROMS has been used in numerous coastal studies with strong currents, turbulent flows and upwelling systems [Marchesiello *et al.*, 2003, 2004; Lutjeharms *et al.*, 2003; Penven *et al.*, 2001a, 2001b]. Those demonstrated the model’s ability to reproduce the

large-scale structures of the thermal and current fields as well as mesoscale characteristics at high spatial resolution.

[7] A detailed description of the model is given by *Marchesiello et al.* [2001, 2003]. Our simulated domain extends over 5000 km zonally and 3800 km meridionally. The northern limit of the domain (2°S) is along the longitudinal axis of the intense part of the southwestward SEC [*Wyrski and Kilonsky*, 1984]. The southern limit (36°S) is located in the weak eastward flow of the southern part of the subtropical gyre. Western and eastern boundaries are respectively 161°W and 116°W to contain the eastern extremity of the STCC and the formation area of the South Pacific Tropical Water (STPW) [*Hanawa and Talley*, 2001] east of the Tuamotu archipelago. The $1/6^{\circ}$ spatial resolution allows it to resolve the first baroclinic Rossby radius of deformation across the domain; 30 vertical levels are used with enhanced resolution near the surface. The 2-min resolution ETOPO2 topography is used, smoothed with a selective Shapiro filter to avoid large pressure gradient errors near the ubiquitous steep topography [*Beckmann and Haidvogel*, 1993]. Because of the ocean bottom sharpness and the small size of the islands and atolls, which some appear as seamounts even in the ETOPO2 topography, a specific mask was built where each model grid point containing a coastline is considered in ETOPO2 as coast.

[8] The model is integrated for 11 years, from 1 January 1993 to 31 December 2004 with a time step of 1800 s. It is forced weekly by satellite wind stress. ERS-1 and -2 1° grid fields (<http://www.ifremer.fr/cersat>) are used from 1993 to 2000 and are spatially interpolated to fit the QuikSCAT 0.5° grid data from 2001 to 2004 (<ftp://ftp.ifremer.fr/ifremer/cersat/products/gridded/mwf-quickcat>). Both fields were interpolated onto the model grid. Fluxes are diagnosed from the monthly 2.5° gridded NCEP (National Center for Environmental Prediction, http://www.cdc.noaa.gov/cdc/data.ncep.reanalysis.html#surface_gauss) reanalysis specified atmospheric variables through bulk formula.

[9] The ROMS model was initialized and forced on its lateral boundaries by 10-day average temperature, salinity, free surface elevation and current fields from the assimilated global model ECCO-2 Massachusetts Institute of Technology General Circulation Model (MITgcm, <http://ecco.jpl.nasa.gov/cgi-bin/nph-dods/datasets/kf040o2>) with spatial resolution of 1° in longitude and 1° to 0.3° in latitude (denser near the equator). The flow is initialized with ECCO-2 MITgcm geostrophic current relative to 2000 m as suggested by *Tomczak and Herzfeld* [1998].

[10] An oblique radiation condition [*Marchesiello et al.*, 2001] is used to estimate the direction of information flux at the open boundaries: if the flux is inward, a nudging term quickly restores the values (time scale in 3 days for temperature and salinity and 10 days for current fields); if the flux is outward the radiation condition is used to extrapolate interior values at boundary points in addition to a weak nudging (1-year time scale out). A sponge layer and a nudging layer are used at the boundary. A sponge layer is a region of increased horizontal viscosity near the open boundaries to absorb disturbances and suppress computational noise associated with the radiation condition [*Palma and Matano*, 1998], while the nudging relaxes model fields toward external values. The layer width is

set to 150 km (i.e., on the order of mesoscale structures); its maximum viscosity value is set at $1000\text{ m}^2\text{ s}^{-1}$. Away from the sponge layer, explicit lateral viscosity and lateral diffusion are null [*Penven*, 2003] (available at http://www.brest.ird.fr/roms_tools). The vertical mixing in the interior and planetary boundary layers is calculated with the non local, K-Profile Parameterization (KPP) [*Large et al.*, 1994].

[11] After a spin-up period of about 1 year, volume integrated quantities oscillate quasiperiodically around an equilibrium value indicating a statistical equilibrium. ROMS output are 5-day averages and are analyzed from 1 January 1994 to 31 December 2004.

3. Topography and Mean Surface Structures

[12] Five main archipelagos create major obstacles to oceanic currents in the domain. All are oriented north-west-southeast (Figure 1). The central Tuamotu Archipelago is the largest with numerous islands and atolls. Aligned with it and to its southeast is the more dispersed Gambier Archipelago. To its north the Marquesas form an important obstacle to the SEC as well. To its west and south, two main island groups separated by wide deep passages form the smaller Society and Austral archipelagos. The extent of the topographic influence on the large-scale circulation depends on the island size and density, which, as can be seen in Figure 1, is highly variable. Mean sea surface height (SSH) and surface geostrophic currents from ROMS are overlain in Figure 1, showing the main features of the surface circulation. The almost zonally oriented SSH ridge around 17°S marks the meridional boundary between the mean surface geostrophic currents. North of this ridge, the westward geostrophic component of the South Equatorial Current (SEC) flows through the Marquesas, Society and North Tuamotu archipelagos. Velocities exceed 30 cm s^{-1} in the northern region and weaken southward, as previously documented [*Wyrski and Kilonsky*, 1984; *Rougerie and Rancher*, 1994]. Following the large-scale anticyclonic gyre circulation of the South Pacific, south of 17°S the surface currents become eastward in the oceanic convergence zone. The SSH and surface geostrophic currents on Figure 1 do not show the intermittent SECC due to the annual averaging.

4. Seasonal Variability

[13] Seasonal variations in atmospheric conditions are significant. The “wet season” occurs during austral summer (November–April, northeasterly winds) associated with the presence of the South Pacific Convergence Zone above the Polynesian archipelagos. Winter is dryer (May–October), with SPCZ remnants and southeasterly winds [*Laurent et al.*, 2004]. We start the seasonal analysis with surface features of the ROMS output, as those benefit from validation against satellite data. The seasonal component of the different signals is obtained by subtracting from the original signal the 2-year Hanning filtered component [*Delcroix*, 1998]. The resulting changes described in this section are summarized in Figure 2.

4.1. Seasonal Sea Surface Anomalies

[14] Seasonally filtered Sea Surface Height Anomaly (SSHA) in ROMS shows two zonally oriented regions of

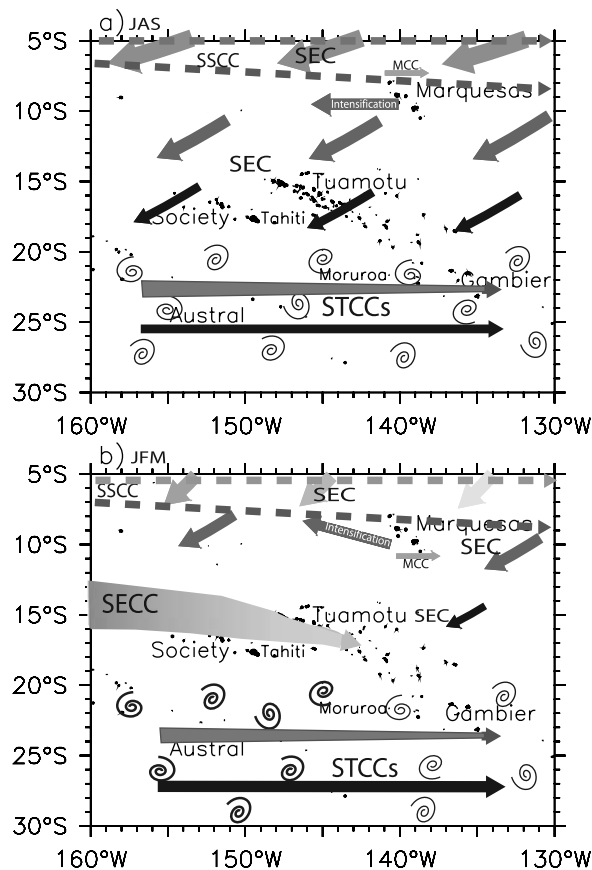


Figure 2. Summary schematic of the main currents in French Polynesia during (top) winter (JAS) and (bottom) summer (JFM). The arrow widths (or line thickness of the eddies in the Subtropical Countercurrent (STCC) area) indicate the relative strength of the current. The arrow direction corresponds to the surface (including Ekman layer) current, and color indicates the relative vertical extension of the currents. The lighter the arrow is, the shallower (or thinner, if it is a subsurface current) the current is. As an example, the northern intense part of the SEC (light gray) is about 125 m deep during winter, whereas the STCCs (black) spread over 500 m. Similarly, the broad dark gray arrow for the SEC represents its intense part, which is vertically limited, unlike its slow part, which flows down to 500 m depth (black arrows). The dashed lines represent the two branches of the subsurface SSCC. The SEC leeward the Marquesas is present all over the year (dark gray).

high variability (Figure 3a, light areas). The first region, between the northern boundary and 6° – 7° S, corresponds to the seasonal variations in amplitude and direction of the northern part of the SEC with SSHA RMS values stronger than 4 cm RMS. Wang *et al.* [2000] identified this area as of high seasonal variability associated with both Ekman pumping (i.e., local wind forcing) and equatorial wave propagation, in contrast to the region south of 10° S which is mostly locally forced. The second large region of high variability, south of 22° S (up to 7 cm RMS) in the Subtropical Countercurrent, has a strong eddy activity which is season-

ally modulated by baroclinic instability according to Qiu and Chen [2004]. There, the variability decreases substantially eastward, marking the tail end of the high variable region of the STCC. In the latitude band between those two regions of high variability, the variability drops (<4 cm RMS) over the broad and less turbulent SEC (7° S to 20° S), as seen on Figure 1. At 15° S, 160° W a small structure of enhanced variability (5 cm RMS) corresponds to the eastern surface limit of the highly energetic South Equatorial Countercurrent [e.g., Qiu and Chen, 2004].

[15] The ROMS SSHA variability is quantitatively similar to satellite data from the AVISO-CLS combined product (Figure 3b). The TOPEX/POSEIDON and ERS-1/2 (TP/ERS) product is combined on a weekly, $1/3^{\circ}$ grid from 1994 to 2004 [Ducet and LeTraon, 2000]. All the aforementioned features appear in the same locations and with comparable amplitudes. The high-resolution ROMS simulation gives a more realistic picture of the turbulent mesoscale STCC than that of the ECCO-2 MITgcm simulation used at the domain boundaries (not shown), in which the high eddy activity was missing.

[16] The annual cycle of the seasonally filtered ROMS SSHA is investigated through an harmonic analysis, following Kessler and Gourdeau [2007]. The first annual harmonic (Figures 4a and 4b) shows that over the French Polynesia the two regions presenting stronger than 2 cm amplitude are located from the northern boundary to 11° S, and south of 24° S with local amplitude up to 8 cm in the

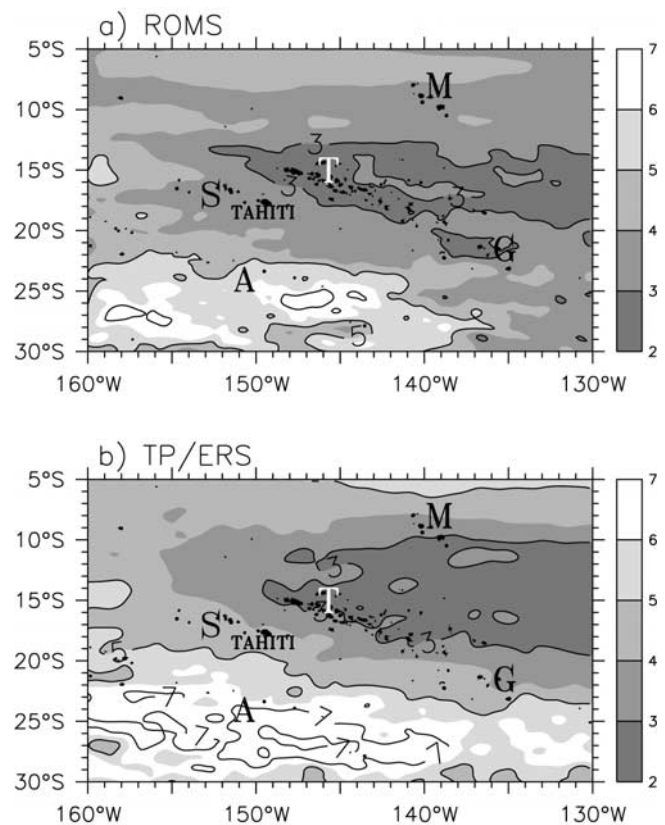


Figure 3. Variability (RMS in centimeters) of the seasonally filtered SSHA from 1994 to 2004 issued from (a) ROMS and (b) TP/ERS. Isolines are drawn every 2 cm RMS. Island names and archipelago initials are indicated.

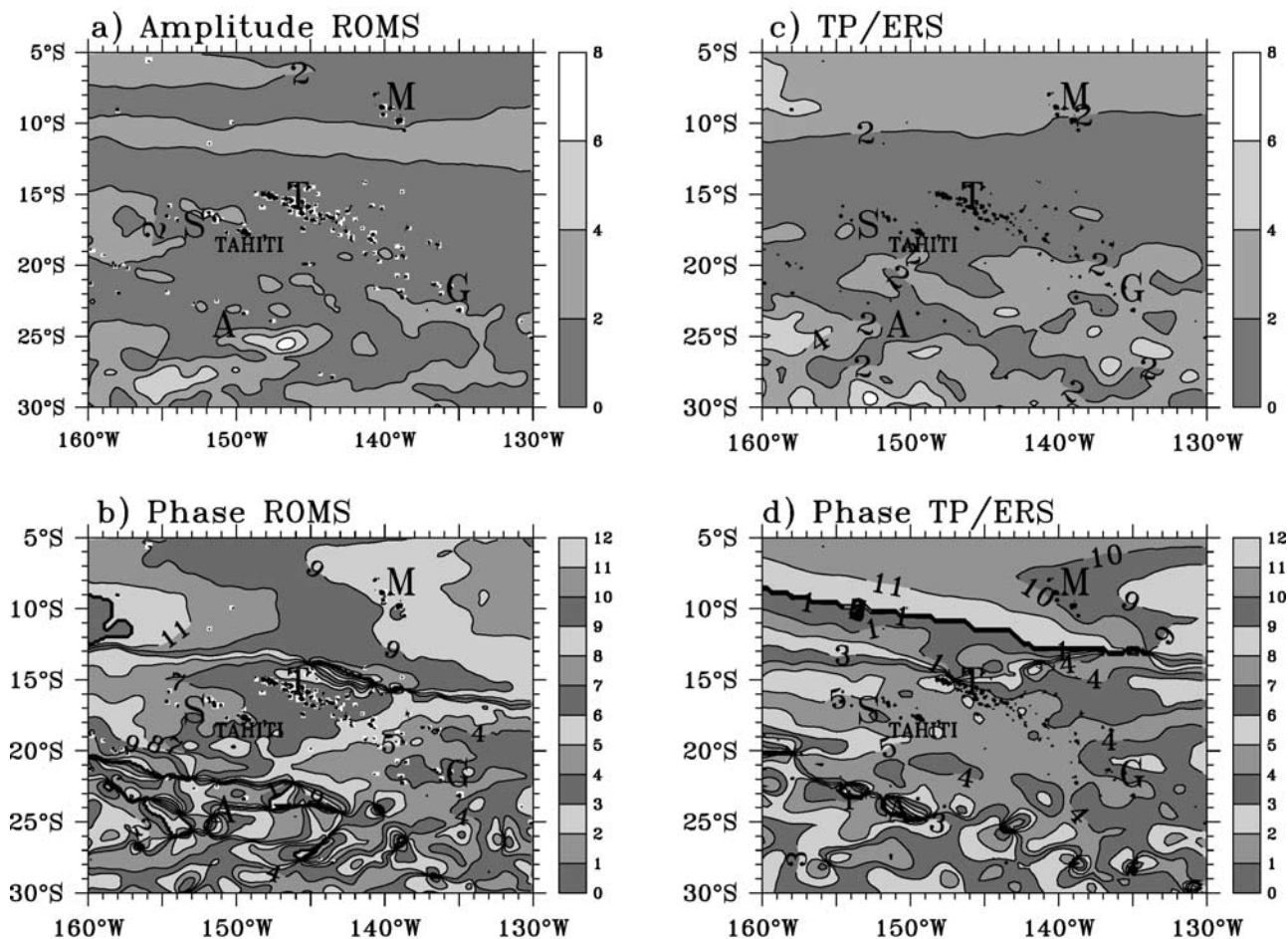


Figure 4. (top) Amplitude of the annual harmonics of the (left) model and (right) combined TP/ERS satellite data in centimeters and (bottom) associated phase of both annual harmonics in months (1, January, etc.).

high-mesoscale-variability area (Figure 4a). ROMS SSHA 1st amplitude and phase annual harmonic are found similar to those of altimetry data and are generally similar in terms of variance percentage and shape of both spatial and temporal components (Figures 4c and 4d).

[17] A very clear westward propagation pattern appears in the northern region in both ROMS and satellite data, with the maximum SSHA occurring in August at 130°W and November/December at 160°W (Figure 4b). This off-equatorial westward propagation north of $12^{\circ}\text{--}13^{\circ}\text{S}$ is driven by equatorial winds and the resonant Rossby waves they generate [Wang *et al.*, 2000; Chen and Qiu, 2004]. A slower propagation pattern appears in the $15^{\circ}\text{--}20^{\circ}\text{S}$ band, starting in May–June at the 130°W . In this region, the thermocline variations are characterized by a dominant local Ekman pumping regime and the sharp phase jump around 12°S results from the boundary of the two different regimes [Wang *et al.*, 2000]. The latitudinal phase jump determines the location of the seasonal SECC [Chen and Qiu, 2004]. Between 5°S and 15°S , altimetry shows meridionally slanted phases resulting from the equatorward increase of wave speed while ROMS shows such slant down to 10°S , followed by a sharp phase shift at 13°S . The reason for this difference is not clear. South of 23°S , both altimetry and

ROMS show a region of eddy-like features with propagations of about 5° over the year.

4.2. Surface Currents

[18] Having introduced the main dynamical features in the SSHA seasonal variability, and evaluated the model skills against satellite data we now examine the variability of the corresponding total (geostrophic plus Ekman) surface currents averaged over the upper 100 m (Figure 5). The average winter currents in ROMS are strongest near the northern boundary, within southwestward SEC with velocities reaching 40 cm s^{-1} at the surface (not shown) and $20\text{--}25\text{ cm s}^{-1}$ in averaged over the upper 100 m (Figure 5a). This winter peak is prominent with a maximum zonal current in July–September, as can be seen on a latitude time diagram averaged over $160\text{--}156^{\circ}\text{W}$ (Figure 5c). During this season, Reverdin *et al.* [1994] using drifting buoys and current meter records also reported a strong zonal current ($4^{\circ}\text{--}6^{\circ}\text{S}$, 150°W). North of 12°S , the zonal component of the SEC is strongest from March to September (up to 20 cm s^{-1} ; Figure 5c). Farther south, the total SEC in the surface layer, which is maximum during winter following the wind enhancement, weakens to the south with $5\text{--}10\text{ cm s}^{-1}$ maximum zonal velocity near Tahiti (17°S , 150°W). From 10°S to 30°S in the Polynesian region, the local

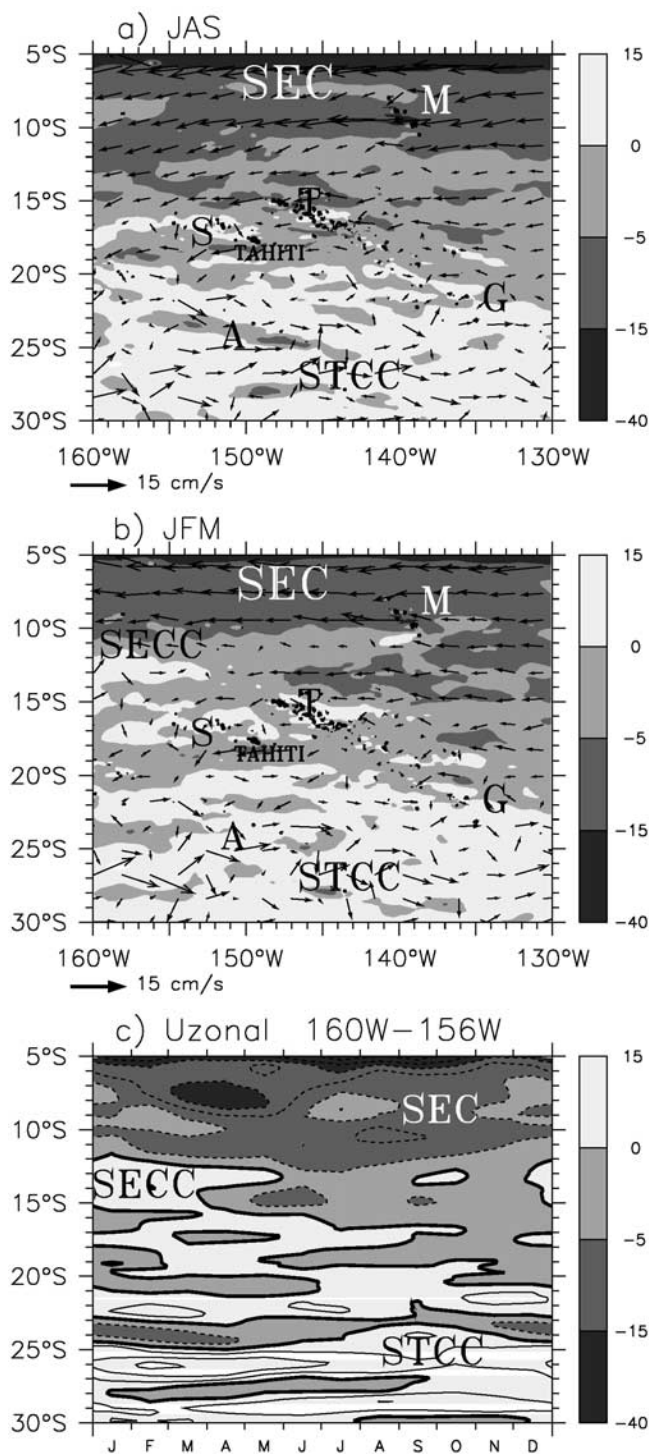


Figure 5. Seasonally filtered surface currents integrated over the 100 upper meters in austral (a) winter and (b) summer issued from ROMS. The zonal component is overlaid in gray scale. Islands are in black, with archipelago initials in bold. The surface current initials are also indicated. (c) To better identify the timing of the different features, a latitude-time diagram of zonal surface current integrated over the 100 upper meters and 160°W–156°W is shown (monthly climatology; positive eastward). Contours are drawn every 5 cm s⁻¹, with the 0 cm s⁻¹ isoline in bold.

Ekman pumping which is the origin of the observed variability of the SEC occurs in June–July [Kessler and Gourdeau, 2007], and leads by 2 months [Wang et al., 2000] the maximum thermocline depth. The maximum in the SEC occurs in September–October, although locally, the Ekman pumping values and variability (Figures 6a and 6c) are smaller than those further west or closer to the equator [e.g., Kessler and Gourdeau, 2007, Figure 4]. The local wind effect (Ekman drift) is to enhance the velocity and add a westward component at the surface as both the zonal and meridional wind stress components are maximum in winter [e.g., Delcroix, 1998] (Figures 6b and 6d). South of 20°S, the surface flow is mainly eastward in the STCC. Velocities reach up to 10–15 cm s⁻¹, and eddies are omnipresent. In the same area near Moruroa atoll (22°S–139°W), Boulanger et al. [1993] observed fluctuating zonal drifts from drifting buoys, alternately eastward and westward with weak velocities (5 to 10 cm s⁻¹) and no clear mean propagation. A wintertime zonal orientation of the surface STCC was reported by Tomczak and Herzfeld [1998] and Martinez et al. [2007] as a northward move of the South Pacific Current (SPC) in the Polynesian waters. Considering the vertical structure, in the next section, we will show that the surface flows are decoupled from the SPC which flows exclusively to the south of our region.

[19] During summer (Figures 5b and 5c), the SEC, integrated over the 100 upper meters, weakens (to 15 cm s⁻¹ at the northern boundary, to 10 cm s⁻¹ around the Marquesas archipelago [8°–11°S] and to 5 cm s⁻¹ farther south). The eastward component corresponding to the SECC can be noticed on a phase diagram (Figure 5c) between December and March, on the western edge of the region from 12°–16°S with velocities lower than 10 cm s⁻¹. Owing to its intermittent presence and latitude shift, the SECC signature is weak on the 3-month time average of Figure 5b. On average, the STCC is stronger (up to 15 cm s⁻¹; Figure 5c) during summer (Figure 5b) than during winter (Figure 5a). A summertime meridional orientation of the surface STCC in the Polynesian waters has been reported in the literature [Tomczak and Herzfeld, 1998; Martinez et al., 2007]. It also appears in ROMS output when only the surface layer is considered, suggesting it represents the southward Ekman transport.

4.3. Seasonal Subsurface Current Variability

[20] We now turn to the description of the vertical structure of the circulation. Along with the omnipresent main currents (SEC, SECC, STCC and the SSCC), ROMS confirms the presence of the occasionally observed Marquesas Countercurrent and eddies which disturb the STCC flow.

4.3.1. South Equatorial Current

[21] The most intense part of the SEC is conspicuous over the north part of the domain, as can be seen on two meridional sections averaged over 160°–156°W and 142°–138°W (Figure 7). The vertical shape of the zonal currents at both longitudes suggests a boundary at 6°–7°S between the intense part of the westward SEC to the north (surface velocities up to 40 cm s⁻¹, as observed in altimetric data [Lagerloef et al., 1999] and in CTD data [Ranacher et al., 1992]) and its weaker part to the south (a 10–15 cm s⁻¹ core around 100 m). During winter, the intense part of the

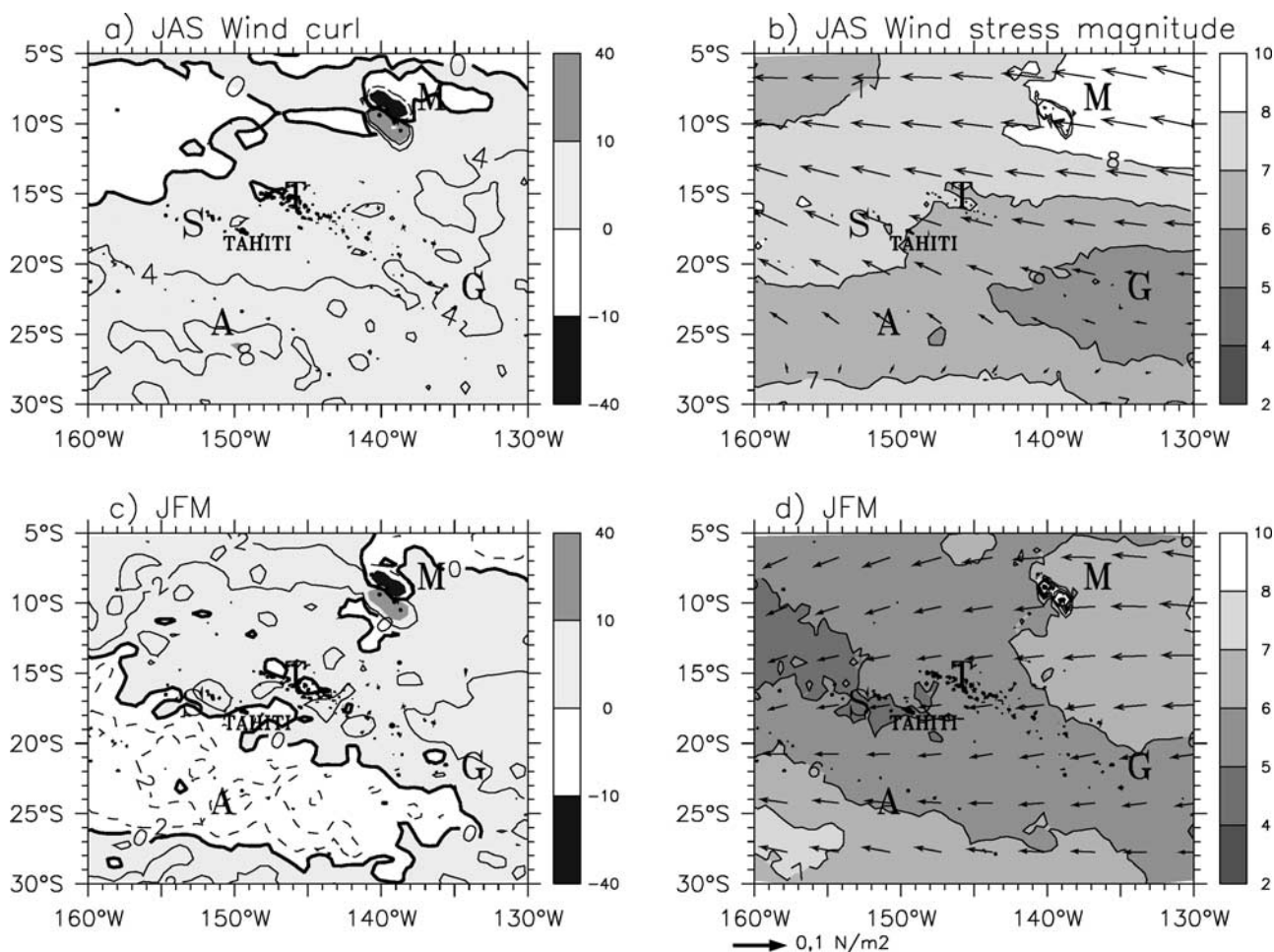


Figure 6. (left) Seasonal wind curl (10^{-8} N m^{-3}) and (right) magnitude of wind stress (10^{-2} N m^{-2}) in austral (a, b) winter and (c, d) summer, respectively. Wind curl and wind stress are derived from the weekly ERS-1 and -2 and QuikSCAT 1° grid. Data from 1993 to 2004 were seasonally filtered as in Figure 3. Islands are in black, with archipelago initials in bold. On the wind curl plots, the bold line is the 0 value, whereas the contours are every $1.10^{-8} \text{ N m}^{-3}$, with dashed lines for the negative values. The cyclonic (Ekman upwelling) curl is negative.

SEC increases with a surface maximum (40 cm s^{-1}) in August–September at 5°S and $142^\circ\text{--}138^\circ\text{W}$ (Figure 7, top right) as previously observed with a current profiler in October 1989 [Rougerie and Rancher, 1994]. It extends southward and deeper, and defining its core by the 20 cm s^{-1} isoline, reaches 125 m at 5°S (close to the 100 m observed by Rougerie and Rancher [1994]) and 7°S at the surface. Its structure is similar at $160^\circ\text{--}156^\circ\text{W}$ (Figure 7, top left) with a weaker shear and southward extension (the surface maximum at the northern boundary reaches 30 cm s^{-1}). During summer, the core of the intense flow is shallower than 50 m and slightly rises from 50 m to 20 m eastward, from $160^\circ\text{--}156^\circ\text{W}$ to $142^\circ\text{--}138^\circ\text{W}$ (Figure 7, bottom). This rise follows the zonal equatorial thermocline slope at 5°S (shown by the density contours on Figure 7, bottom).

[22] South of 6°S , the SEC in ROMS has a mean value near 5 cm s^{-1} , and core velocities larger than 10 cm s^{-1} , as also observed during the Shuttle [Wyrki and Kilonsky, 1984]. During winter, due to the 2 months lead [Wang et al., 2000] of maximum downwelling curl in June–July

[Kessler and Gourdeau, 2007], the SEC intensifies and the stronger ($>5 \text{ cm s}^{-1}$) flow occupies a broad latitude band, all the way to 17°S at the surface and spans 10°S to 12.5°S at 300 m (Figure 7, top). During summer at $160^\circ\text{--}156^\circ\text{W}$ (Figure 7, bottom left) ROMS shows that the stronger part ($>5 \text{ cm s}^{-1}$) of the flow reaches only 12°S in a surface (0–25 m) and subsurface layer (50 m to 200–250 m). At $142^\circ\text{--}138^\circ\text{W}$ both layers extend further south (16°S). The observed variations in the SEC are consistent with the seasonal changes in the surface geostrophic flow, with a strong SEC during the second half of the year [Kessler and Gourdeau, 2007] and a maximum (minimum) in winter (summer) in agreement with drifter observations from Reverdin et al. [1994].

4.3.2. Southern Subsurface Countercurrent

[23] In the northern part of the domain and below 250 m, the SSCC or Tsuchiya jet [Tsuchiya, 1972], flows as an eastward subsurface countercurrent (Figure 7). It is remarkably steady and extends across the region as previously observed across the entire Pacific Ocean by Johnson and

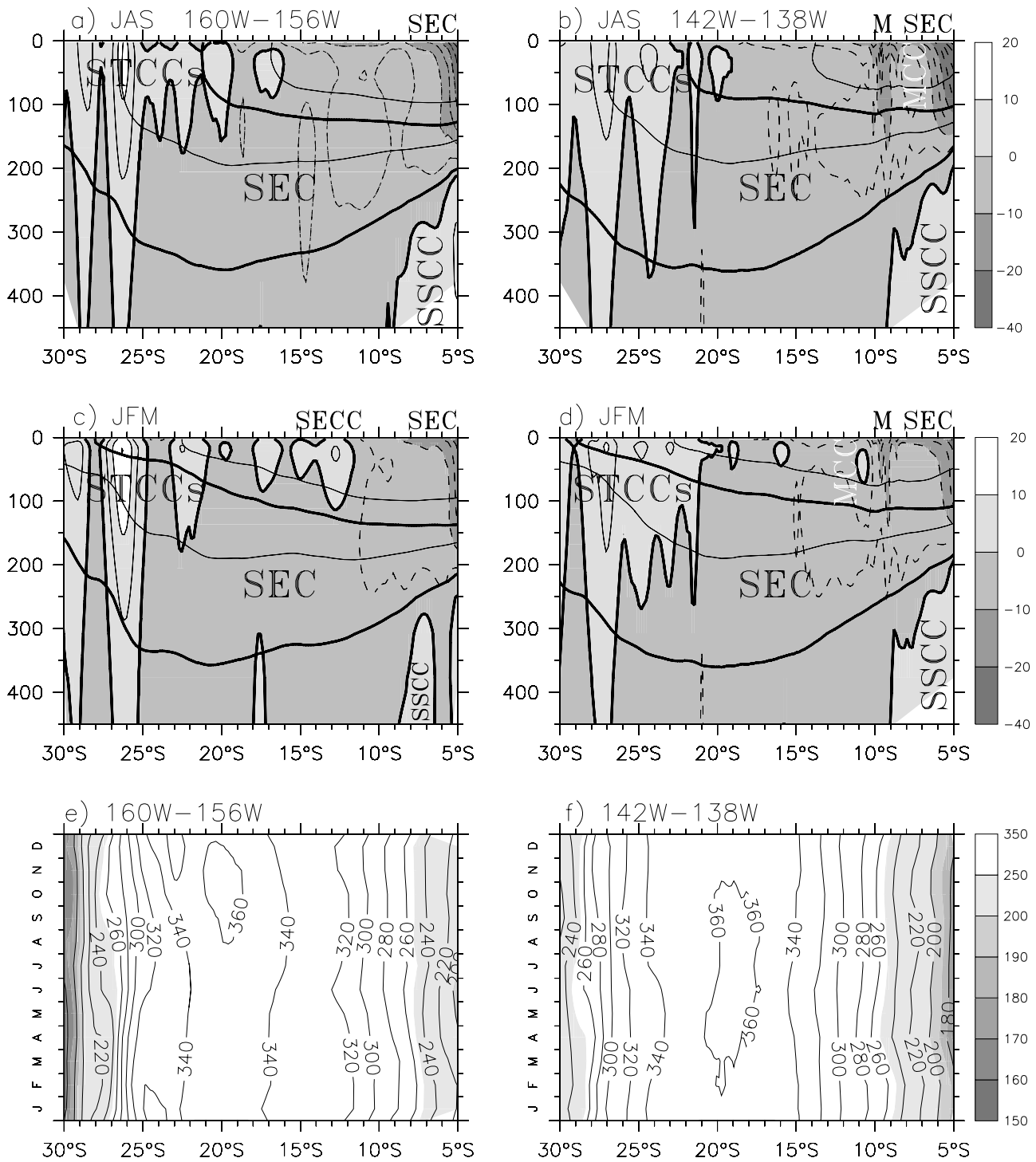


Figure 7. ROMS mean zonal velocity (cm s^{-1}) in (top) winter and (middle) summer, averaged over (left) 160° – 156° W and (right) 142° – 138° W. At 142° – 138° W, the Marquesas archipelago (“M”) is indicated on the top. The currents are indicated in bold: SEC, SECC, SSCC, Marquesas Countercurrent (MCC), and the westward and eastward branches belonging to the STCC, reported as “STCCs.” The intense part of the SEC is indicated in black at top right. Contours are plotted every 5 cm s^{-1} , with the 0 cm s^{-1} isoline in bold. Contours of density are plotted every 1 kg m^{-3} , with the 24 and 26 kg m^{-3} isopycnals in bold. (bottom) Latitude-time diagrams of the depth (in meters) of the isopycnal 26 kg m^{-3} are shown. Contours are drawn every 20 m .

Moore [1997]. The ROMS SSCC appears to have two branches: a “primary” jet close to the equator below 200 m (at the northern boundary on Figure 7) and a “second-

ary” one below 250 – 300 m and farther south all the way to 8° – 10° S. If they appear well separate on ROMS vertical sections for a given longitude, on Figure 7, due to the 4°

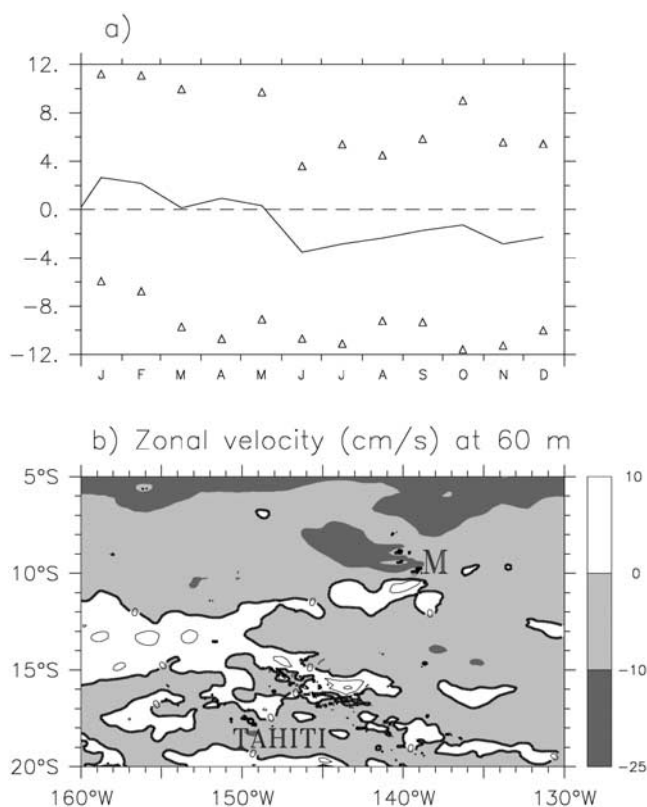


Figure 8. (a) Monthly climatology of the seasonal zonal currents (in centimeters per second) in the core of the SECC (60 m deep), at 160°W and averaged over 12°–16°S (line) and its variability (± 1 standard deviation, triangles). The dashed line is the 0 cm s⁻¹ line. (b) January zonal velocity (in centimeters per second) at 60 m depth; contours are drawn every 5 cm s⁻¹, and the 0 cm s⁻¹ contour is in bold. Marquesas archipelago initial is indicated in bold.

longitudinal average they are distinguishable because of their upper limit and latitude location. From the Shuttle data, *Wyrki and Kilonsky* [1984] reported these two SSCC branches, the primary one centered at 4°S, 250 m and the secondary one at 7°S, 320 m. In ROMS, the SSCC is broader at 142°–138°W than at 160°–156°W consistent with *Furue et al.* [2007], who reported an eastward transport increase. The secondary jet in ROMS shifts poleward and gets shallower as it flows eastward, following the shoaling of the tropical pycnocline (see the 26 kg m⁻³ isopycnal in Figures 7a–7f). The origin and dynamics of the SSCCs is controversial, with several competing theories [*Johnson and Moore*, 1997; *McCreary et al.*, 2002; *Ishida et al.*, 2005; *Jochum and Malanotte-Rizzoli*, 2004].

4.3.3. South Equatorial Countercurrent

[24] Extending between 9 and 12°S and from New Guinea to nearly 150°W [*Reverdin et al.*, 1994; *Chen and Qiu*, 2004] the SECC is poorly documented east of 160°W. Figure 7c shows the vertical structure of this eastward countercurrent which is a wind driven Sverdrup flow [*Chen and Qiu*, 2004]. It appears in early December and lasts until mid-March (Figure 5c). The seasonally averaged SECC in ROMS appears near 160°–156°W between 12°S and 16°S (Figure 7, bottom left) and is located during summer where

the wind stress is minimum (Figure 6d) as also reported by *Tomczak and Godfrey* [1994].

[25] The monthly variations of the 12°–16°S average zonal velocity at 160°W (Figure 8a) and at 60 m (which is in the SECC core) show that the SECC appears in the Polynesian water in January with a 3 ± 8 cm s⁻¹ mean velocity and disappears from April to December. At its peak in January, the SECC reaches 150°W from 12°S to 16°S with 5 cm s⁻¹ velocities (Figure 8b) with a maximum vertical extension reaching 120 m (not shown). The above description of the SECC is consistent with *Kessler and Taft's* [1987] observations from XBT data, west of 160°W. The position of the SECC may fluctuate over a large band of latitude [10°–16°S]. Such displacements were also observed during Hydropol (one to two CTD sections a year between 1986 and 1989 near 140°W [*Rancher et al.*, 1992; *Rougerie and Rancher*, 1994]). The seasonal ROMS velocities are stronger than the 2 cm s⁻¹ mean velocities reported by *Wyrki and Kilonsky* [1984] but consistent with the Shuttle results [*Eldin*, 1983; *Rougerie and Rancher*, 1994]. Their lower values are due according to them to a misleading annual temporal average that conceals the SECC in the dominant westward flow.

4.3.4. Marquesas Countercurrent

[26] The satellite-derived wind reveals that a wind stress curl dipole is localized around the two highest (approximately 1210 m) Marquesas Islands, Nuku Hiva (8.5°S, 140°W) and Hiva Oa (9.5°S, 138.6°W; Figures 6a and 6c). The dipole, with negative curl in the north and positive vorticity in the south, is similar to the one observed around the Hawaiian Islands or the Cabo Verde island [*Xie et al.*, 2001; *Qiu and Durland*, 2002; *Chavanne et al.*, 2002]. Below the north lobe of this wind curl dipole, a westward oceanic jet around the Marquesas Islands ridge (8°–11°S), 140°W in Figure 8b) is modeled for the first time. Isopycnals are uplifted on the edges of the islands (Figure 7, right). The jet extends from the surface to 175 m with velocity up to 20 cm s⁻¹ (Figures 7b, 7d, and 8b). The jet is detected in the wake of the Marquesas ridge to 147°W (Figure 8b). It is stronger during winter, with a zonal direction, than during summer, with a northwestward direction.

[27] Figure 7 (right) shows that north and south of this westward jet are either an eastward countercurrent or a weakening of the westward flow. They both are about 100–200 km wide and 100 m deep. The eastward countercurrent in ROMS, referred to the Marquesas Countercurrent, flows with 5 cm s⁻¹ speed and moves meridionally according to the season. During austral summer, it is south of the archipelago (Figures 7d and 8b). As it extends approximately over 500 km in longitude, it flows close to the SECC. Our results show that the MCC is a permanent feature of the current system around the Marquesas and not an erratic component of the SECC as previously reported in the literature [*Eldin*, 1983; *Rancher et al.*, 1992; *Rancher and Rougerie*, 1995]. During winter the MCC (Figure 7b) is found north of the archipelago and its extension in longitude is over 2°. As the surface SEC reinforces, the MCC flow becomes subsurface, from 30 m to 100 m.

4.3.5. Subtropical Countercurrent

[28] At 160°–156°W, the STCC is represented as a mean eastward flow south of about 20°S (23°S) to 30°S, and from the surface to 250 m (325 m) (Figures 7a and 7c). It is

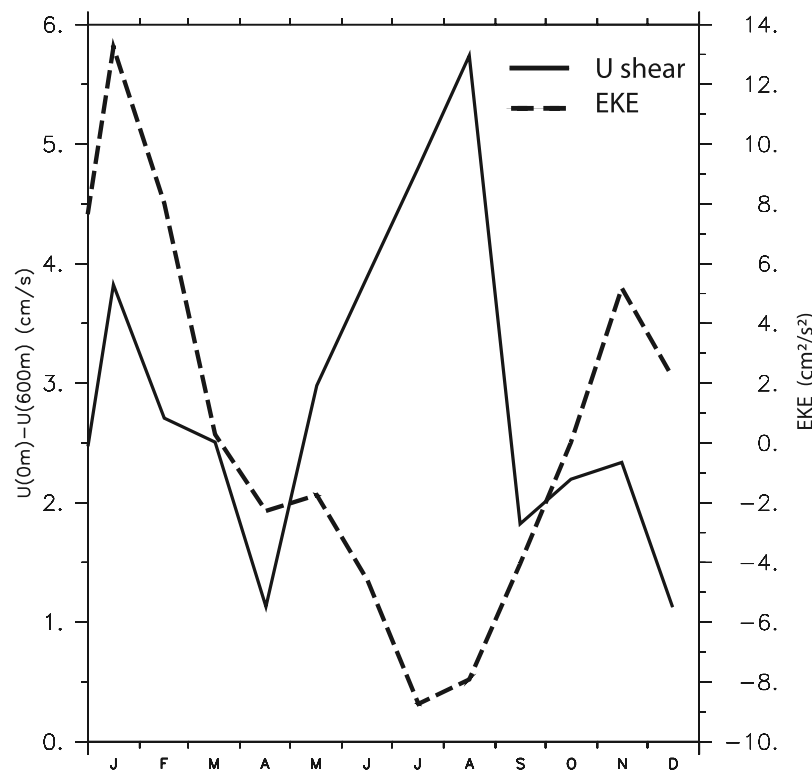


Figure 9. Zonal velocity shear (solid line) between 0 and 600 m averaged over the STCC-SEC region of 21° – 29° S and 160° – 140° W. The zonal flows are calculated from the seasonally filtered ROMS output. The dashed line shows the monthly eddy kinetic energy time series in the STCC region derived from the seasonally filtered ROMS surface geostrophic currents.

bordered to the north and underneath by the westward flowing SEC. As we have seen at the beginning of this section, the regional model dynamics reproduce the observed eddy activity in the STCC region (not shown), unlike ECCO-2 MITgcm. Alternating eastward and westward branches flow south of 20° S in the STCC and down to 300–500 m (Figure 7) as reported by *Rancher et al.* [1992] with surface velocities higher than 10 cm s^{-1} along their Marquesas-Austral sections, although they did not identify those currents as part of the STCC. The westward branches in ROMS can be noticed where downward tilts occur on the isopycnals (Figures 7a–7d). East of 135° W and until the eastern boundary of the ROMS domain (116° W), the eddy activity and those associated westward/eastward perturbations decrease in the STCC, which flows at 116° W over the upper 300 m from 23° S to 30° S (not shown).

[29] On large scales, the strength of the surface STCC has been shown to be strongly modulated by the seasonal surface winds and buoyancy forcing [*Morris et al.*, 1996], but we did not find any report of a clear seasonal variability in French Polynesia where the STCC remains little observed. In ROMS, west of 135° W, the eddy kinetic energy (EKE) shows clear seasonal signal (Figure 9). Averaged from 21° to 29° S and 160° – 140° W, seasonal EKE is maximum in January lagging the maximum STCC-SEC shear by about 4 months. These amplitude and time lag are also given by *Qiu and Chen's* [2004] diagnostic over the region 21° – 29° S and 180° – 160° W. In agreement with their results, the observed EKE seasonal variation in the STCC is consistent with baroclinic insta-

bilities. Westward and eastward flows in the STCC have the strongest velocities in their cores during summer, at both 160° – 156° W and 142° – 138° W (Figure 7, middle), when the maximum EKE occurs (Figure 9).

5. Impact of El Niño 1997–1998 on the Circulation

[30] Having considered the mean conditions and seasonal evolution in both our simulation and the data used to validate it (Figures 1 and 2), we now examine variability on interannual time scales. The 1997/1999 ENSO event is recognized as one of the strongest of the 20th century [*McPhaden*, 1999], and had major impacts on the wind field and surface currents in French Polynesia [*Picaut et al.*, 2002; *Martinez et al.*, 2007]. The main basin-scale changes induced by El Niño/La Niña events are briefly recalled before analyzing the surface and subsurface current 1997/1999 ENSO variability. Westerly (easterly) wind anomalies over the central equatorial Pacific precede the onset of El Niño (La Niña) events [*Delcroix*, 1998; *McPhaden*, 1999; *Picaut et al.*, 2001]. Along the equator at the eastern edge of the warm pool, the warm water spreads eastward, advected by currents that are induced by both a succession of westerly wind bursts and the resulting equatorial wave generation [*McPhaden*, 1999; *Picaut et al.*, 2002]. Further east, the thermocline deepens and the source of upwelled cold water disappears influencing local surface fluxes and warming the surface waters [*Kessler and McPhaden*, 1995]. The sea level is higher (lower) than average in the eastern

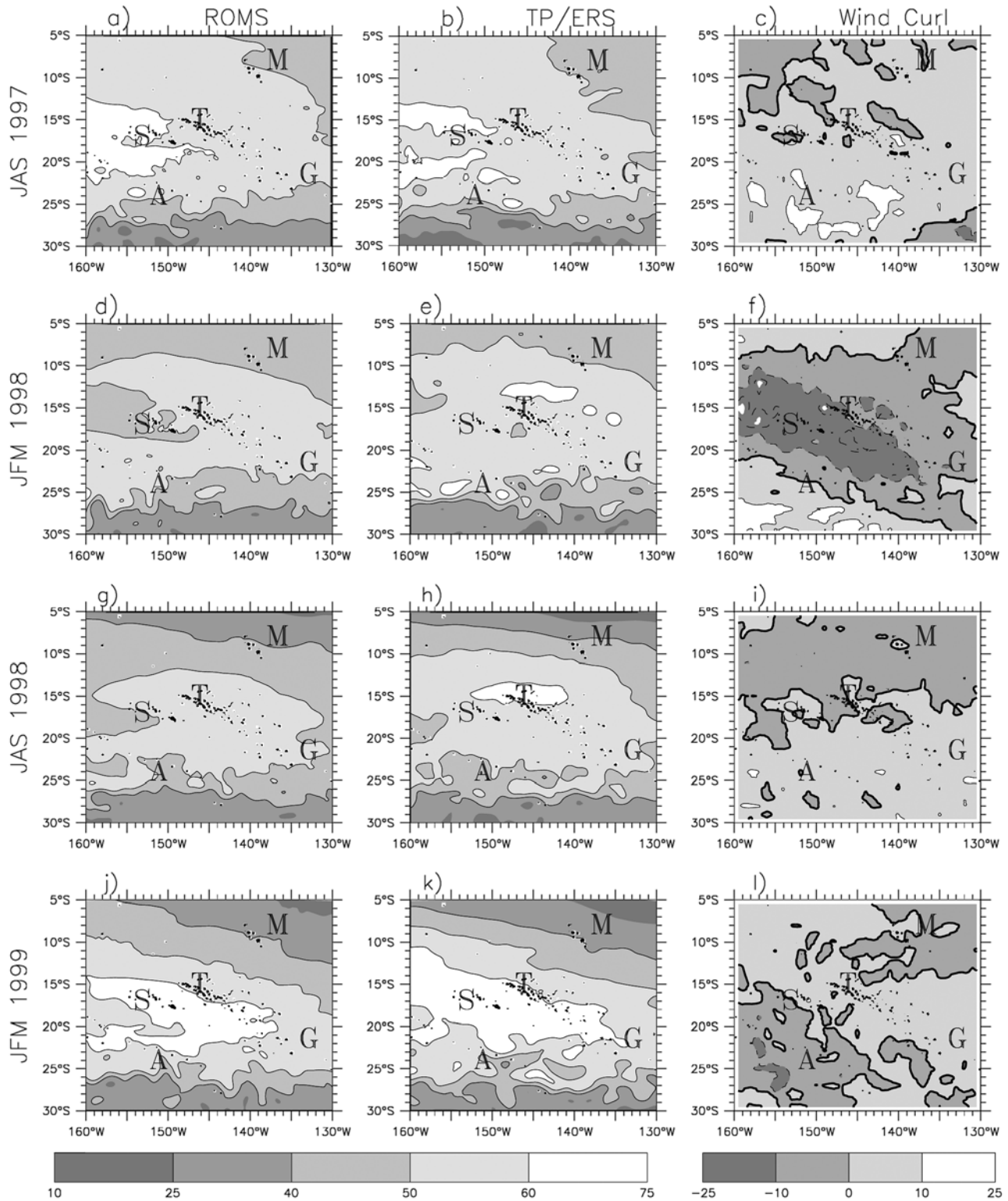


Figure 10. (left) Three-month average original ROMS SSH (in centimeters), (middle) TP/ERS SSH (in centimeters), and (right) satellite-derived wind curl (10^{-8} N m^{-3}) during (a–c) El Niño in winter 1997, (d–f) El Niño in summer 1998, and La Niña in (g–i) winter 1998 and (j–l) summer 1999. Contours are drawn every 10 cm for the SSH and every $1 \cdot 10^{-8} \text{ N m}^{-3}$ for the wind curl.

half of the basin during El Niño (La Niña) events. This sea level zonal change between El Niño and La Niña is referred to a *seesaw* structure [Delcroix, 1998] and is almost in phase with the southern oscillation index (SOI). Although those

variations are predominantly in the equatorial band, their effects were reported down to $15^{\circ}\text{S}–20^{\circ}\text{N}$ [Delcroix, 1998; Picaut et al., 2002] with the pivot of the seesaw in the Polynesian waters. The pivot is defined as the region of

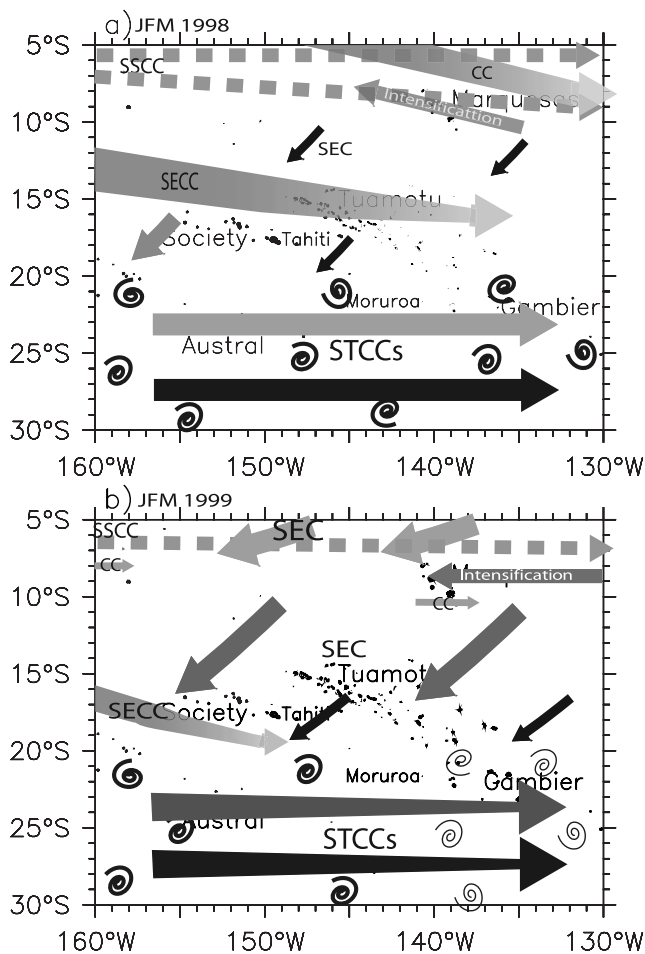


Figure 11. As in Figure 2, but during (top) the El Niño event in JFM 1998 and (bottom) the La Niña event in JFM 1999.

transition between the southeast and the southwest Pacific variability [Picaut *et al.*, 2002]. Off the equator, ENSO changes are concomitant with the SPCZ which moves northeastward (southwestward) and strengthens (weakens) during El Niño (La Niña) [Vincent, 1994]. The enhancement of the SPCZ during El Niño comes with a strengthened SECC and a reduced SEC in the western Pacific [Kessler and Taft, 1987], because the associated anomalous Ekman pumping depresses the thermocline toward the equator, thereby increasing the SSHA and modifying the corresponding geostrophic currents [Delcroix, 1998]. Keeping in mind these large-scale changes, we now examine the 1997/1999 ENSO changes in the Polynesian waters as simulated in ROMS.

5.1. Sea Surface Height Anomalies During the 1997–1999 El Niño–Southern Oscillation Event

[31] We selected four snapshots (Figure 10) of the 3-month averaged original SSH field to characterize the influence of El Niño: JAS 1997 (Niño onset); JFM 1998 (fully developed El Niño); and La Niña: JAS 1998 (fully developed La Niña) and JFM 1999 (end of La Niña). During El Niño, in winter 1997 (Figure 10a) and summer 1998 (Figure 10d), the high (low) SSHA in the northeastern (southwestern) region of French Polynesia decreased both the zonal and meridional SSH gradients north of 20°S (see Figure 1 for the mean values), and showed the southward

extension of the equatorial zonal seesaw structure. In JFM 1998, as the upward wind curl strengthened (Figure 10f), the thermocline tilt at the western boundary induced a trough of SSH (negative SSHA) between 12°S and 16°S (Figure 10d). During La Niña, in JAS 1998 and JFM 1999 (Figures 10g and 10j), the SSHA became negative north of 15°S and the SSH meridional gradient increased. In JFM 1999, the upward wind curl region moved to the south (Figure 10l) and so did the negative SSHA (decrease of SSH) region centered on 11°S (Figure 10g). The comparison of the modeled 1997/1998 El Niño and 1998/1999 La Niña event SSH signals with the TP/ERS data gave similar variations (Figure 10, middle).

5.2. Surface and Subsurface Circulation During the 1997–1999 El Niño–La Niña Event

[32] During El Niño and La Niña, Polynesian currents were modified over the entire domain. We describe below the changes in the vertical structure of each current with the 1997/1999 ENSO conditions. These are summarized in Figure 11.

5.2.1. SEC

[33] During El Niño in winter 1997 (Figures 12a and 12b), in the northern region the SEC weakened with respect to its seasonal average following the decrease of meridional SSH gradient seen in the previous section and its intense part at the northern boundary narrowed and got shallower. In JFM 1998 (Figures 12c and 12d), north of 15°S, the SEC velocity was down to 5 cm s^{-1} associated with the seesaw reversing equatorial conditions. For instance, at 5°S and 142°–138°W, the 23 kg m^{-3} isopycnal was deeper (90 m) than during a normal summer (when it outcrops at 6.5°S). This weakening was also observed in the SEC geostrophic transport by Kessler and Taft [1987] during the onset of El Niño in November 1982 west of 160°W and was attributed to the northward shift of the SPCZ. On the western region between 15°S and 20°S (Figure 12c), some flow of the SEC reached 20 cm s^{-1} at the surface and 5 cm s^{-1} down to 300–400 m. Such an increase during El Niño was also reported in observations in March 1987 by Rancher *et al.* [1992].

[34] During La Niña, the intense part of the SEC strengthened following the increase in the SSH slope (Figures 10g and 10j) at the northern boundary with surface velocity up to 40 cm s^{-1} at 142°–138°W (Figures 12e–12h) when the 23 kg m^{-3} isopycnal shoaled (35 m, versus 50 m during a normal winter) at 5°S. The SEC extended farther south (8°S) and deeper (75 m) at 142°–138°W than at 160°–156°W (6°S and 50 m deep). The 5 cm s^{-1} SEC isotach extended about 3° farther south and 50 m deeper during both winter 1998 and summer 1999 than during “normal” season (12.5°–16°S and 250–300 m; Figure 7). In JFM 1999 (Figures 12g and 12h), the SEC at the northern boundary was stronger than during normal conditions and the 20 cm s^{-1} isoline was about 75 m deeper than during a normal summer.

5.2.2. SSCC

[35] During El Niño (Figures 12a–12d), the SSCC core shallowed: in JAS 1997, its secondary jet upper limit was about 250 m versus 325 m in normal conditions at 160°–156°W. In JFM 1998, the SSCC primary (secondary) jet upper limit shallowed up to 150 m (200 m) (Figures 12c and 12d). During La Niña in JAS 1998, the jets still had shallow

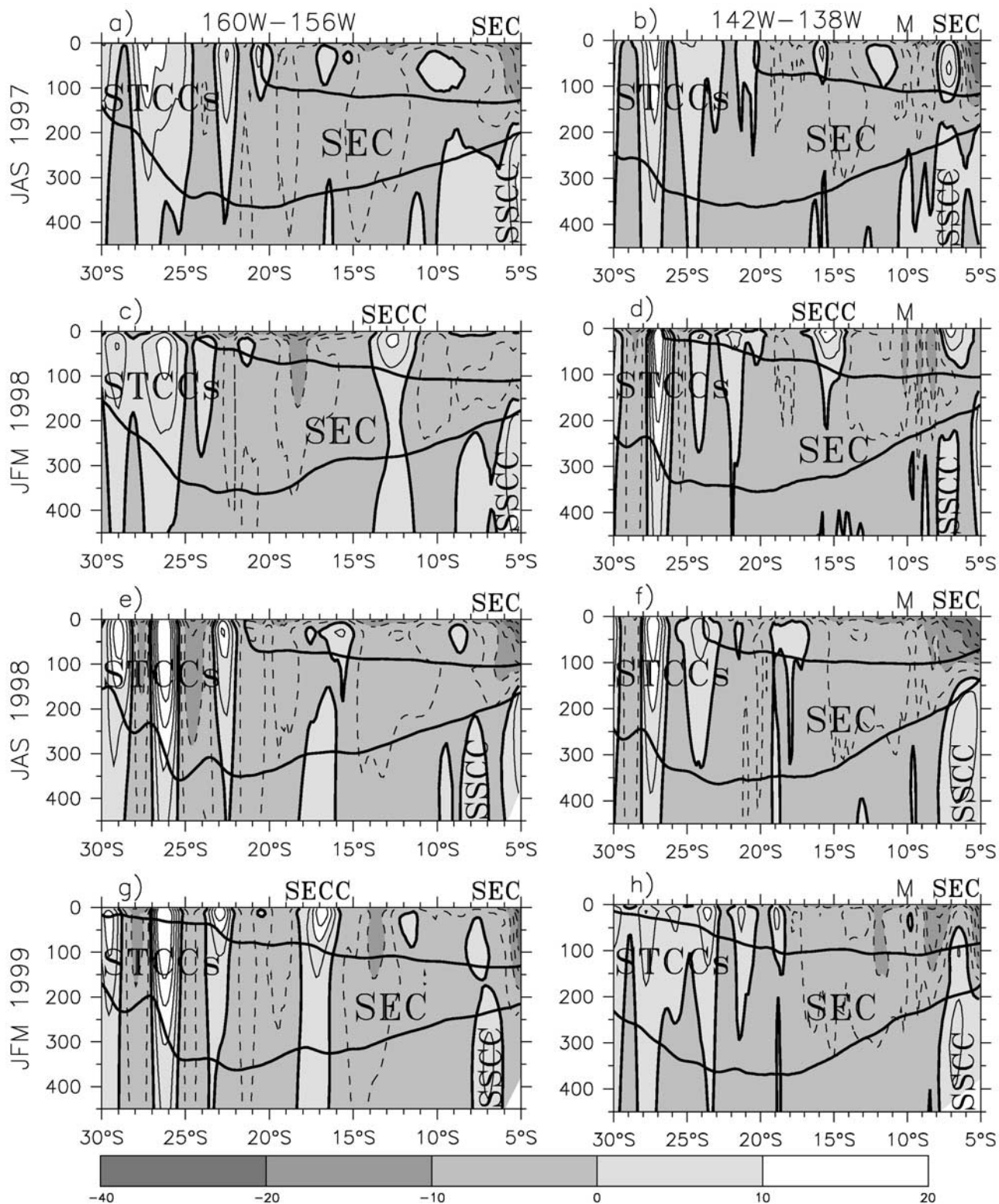


Figure 12. ROMS zonal velocity (cm s^{-1}) during (top) El Niño in winter (JAS) 1997 and summer (JFM) 1998 and (bottom) La Niña in winter (JAS) 1998 and summer 1999. Longitudinal averaged (left) over 160° – 156° W and (right) over 142° – 138° W. Contours are plotted every 5 cm s^{-1} , with the 0 cm s^{-1} isoline in bold. The 24 and 26 kg m^{-3} isopycnals are in bold.

upper boundaries (Figures 12e–12h). In JFM 1999, the primary jet had moved northward out of the region (not shown). It was flowing deeper than during normal conditions

below the strongest part of the SEC near 6° S. A weakening of the SSCC between 150 and 500 m was observed from late 1997 to mid 1998, followed by a strengthening until mid

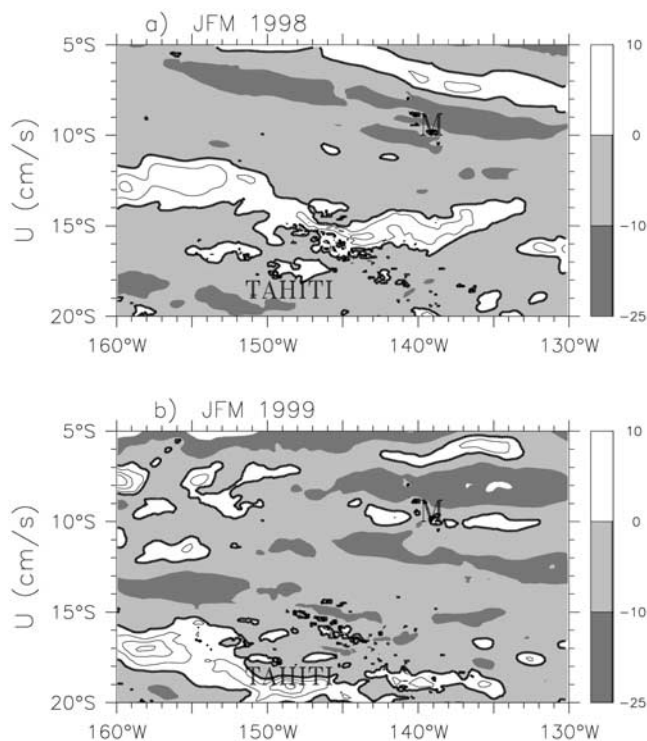


Figure 13. Same as Figure 8b, except during (a) El Niño (first trimester of 1998) and (b) La Niña (first trimester of 1999). Contours are drawn every 5 cm s^{-1} .

1999, for its resolved component (south of 5°S) (time series not shown). As we have seen earlier there are still controversies on the mechanisms that drive the SSCC at a seasonal level. We are not able to propose any mechanism that drives the interannual variability of the SSCC. A study at the scale of the Pacific Ocean would be needed.

5.2.3. SECC

[36] In JFM 1998 (Figures 12c and 12d), following the strengthening of the upward wind curl (Figure 10f) and associated trough in the SSH field (Figure 10d), the SECC was stronger than during a normal summer with velocity up to 15 cm s^{-1} and centered around 13°S . At 160°W it spanned a 3° latitude band centered on 13°S (Figure 13a); it reached 190 m depth till 135°W (not shown) and followed the northwest-southeast orientation of the upward wind curl region revealed by Figure 10f. This orientation was consistent with its 5° – 10°S position found farther west along the Central Pacific tracks during the other major El Niño event in early 1983 [Kessler and Taft, 1987]. In JFM 1999, the upward wind curl region has moved southwestward (Figure 10l) compared to a normal summer and the SECC was near 17°S (Figures 10j, 12g, 12h, and 13b) and down to 170 m (not shown) with surface velocities up to 20 cm s^{-1} .

5.2.4. MCC and Surrounding Countercurrent

[37] From JAS 1997 to JFM 1999, westerly wind anomalies occurred during El Niño and the easterly wind field strengthened during La Niña. As a consequence, the wind curl dipole around the Marquesas Islands presented in the previous section disappeared (Figure 10, right) and only reappeared in July 1999. Consequently, the MCC and westward intensification associated earlier with the dipole were no longer visible. Neither was the isopycnal upward

tilt on the island edges. The wind irregularities around the Marquesas Islands produced several current anomalies including eastward countercurrents during the El Niño event (Figures 12a–12d). In JFM 1998 (Figure 13a), an eastward flow entered the domain, through the northern boundary at 155°W , to 130°W . This countercurrent flowed north of the Marquesas archipelago at 142° – 138°W (Figure 12d) between 6°S and 8°S with velocities up to 15 cm s^{-1} and at level as deep as 80 m. During La Niña in JAS 1998 and JFM 1999 (Figures 12f and 12h), as the SSH gradient increased (Figures 10g and 10j), the SEC increased and the countercurrent disappeared. The strong westward velocities noticed around the islands at 142° – 138°W (Figure 12, right) appeared farther east of the Archipelago (Figure 13).

5.2.5. Eastward Countercurrent at 15°S – 17°S

[38] During La Niña in JAS 1998, a trough in SSH from 160°W to 150°W near 15° – 17°S (Figure 10g), around the location where the SECC is usually seen, induced an eastward countercurrent flowing over the 100 upper meters with velocities up to 10 cm s^{-1} (Figure 12e).

5.2.6. STCC

[39] During the El Niño event (Figures 12a–12d), following the strong SSH variability (Figures 10a and 10d), induced by the mesoscale SSHA activity, the branches in the STCC reinforced with velocities up to 25 – 30 cm s^{-1} for the upper 350 m and the upward tilt amplitude in the isopycnals was stronger. This strengthening during both El Niño and La Niña events has also been reported at the surface by Martinez *et al.* [2007]. It is interesting to notice that during the 1987 ENSO event Rancher *et al.* [1992] also observed deep and narrow (1° in latitude) eastward countercurrents close to 20°S with velocities reaching 30 cm s^{-1} . During La Niña event (JAS 1998), the STCC branches remained strong (Figures 12e and 12f). In summer 1999 (Figure 12h) they weakened at 142° – 138°W and farther east as the tilt amplitude in the isopycnals decreased.

6. Summary and Discussion

[40] To date, our knowledge of the circulation in French Polynesia has been based on sparse data in time and space. A real seasonal pattern was difficult to identify as the seasonal SSH and current signals in the central South Pacific, south of the near-equatorial region, are quite weak compared to those further west [Wang *et al.*, 2000; Kessler and Gourdeau, 2007]. This is due to both weak wind variability (same papers) and a location which is not reached by remotely forced Rossby waves coming from a region with strong forcing farther east. The use of a high-resolution model, validated with satellite data, allowed the authors to describe for the first time and for the entire region important aspects of the seasonal and the 1997/1999 ENSO variability of currents in the French Polynesian Economic Exclusive Zone. This allowed in particular the identification of a Marquesas lee Countercurrent which seems related to a wind curl dipole, the characterization of the intermittent intrusion of the SECC during austral summer, and the structure of the STCC in Polynesian waters.

[41] The main patterns of seasonal variability are displayed on Figure 2. During wintertime (JAS; Figure 2a) as trade winds increase, the SEC is most intense over the 0–200 m layer. During austral summer (JFM; Figure 2b), the

SEC weakens. The SECC appears in the Polynesian waters north of the region of upward Ekman pumping. As a result, the SEC is confined north of 15° – 18° S at the surface, while its depth extent remains similar below the SECC (about 100 m). The SECC enters the region at 160° W between 12° S and 16° , reaches 150° W and dissipates southeastward. Near the Marquesas Islands, the eastward Marquesas Countercurrent appears to be a permanent feature. We find that the MCC is associated with a symmetric weakening of the SEC on the other side of the Marquesas Islands, and a leeward westward jet which is probably caused by perturbations in the wind curl by orographic effects. The MCC flows north of the Marquesas Islands in winter while a weakening of the SEC occurs on the southern side; and vice versa in summer. South of 20° S, the STCC, which has not been very well described in this area, flows to the east just above the westward flowing SEC (Figure 2). Strong eddy activity is observed in the STCC with EKE seasonal variation likely generated by baroclinic instabilities.

[42] Major changes to this seasonal cycle were noticed during El Niño 1997/1998. During the fully developed El Niño in JFM 1998 (Figure 11a), due to the reversing of the equatorial winds, the seasonally strong SEC weakened. The cyclonic wind curl (upward Ekman pumping), moved northeastwardly and strengthened. Those changes modified the SSH and thermocline slopes, resulting in an eastward SECC, stronger and deeper than the seasonal current. The SEC was confined between eastward flows. The wind curl dipole around the Marquesas Islands disappeared as did the MCC and leeward jet, while a countercurrent independent from the so-called MCC is observed around the Marquesas Islands. Further investigations are however necessary to fully understand the mechanisms of this eastward countercurrent. To the south, the SSHA variability associated to mesoscale eddies strongly increased and the STCC intensified.

[43] During La Niña, in JFM 1999 (Figure 11b), the trade winds reinforced. The SEC strengthened and countercurrents started to retract away from the region. The region of upward Ekman pumping moved southwestward and weakened inducing a similar migration of the SECC. Local countercurrents remained in the northern region due to changes in the wind curl and SSH fields. The wind curl dipole and associated Marquesas jets were still absent and only reappeared in July 1999. To the south, the STCC was still present but started to weaken especially in the eastern part of the domain.

[44] In JFM 2000, the normal situation is settled back regarding the SECC position, the MCC reappearance, the east-west density slope north of 15° S (and so the SEC strength as well as the disappearance of the countercurrents in this region).

[45] The dynamics that drives the different currents can be summarized as follows: the main current, the SEC is part of the large-scale South Pacific wind-driven gyre and follows its seasonal cycle. Specific features modulate its strength and create two large countercurrents, the STCC and the SECC which both enter the area from the west. The SECC appears in the area only during 3 summer months. This is a wind driven Sverdrup flow whose position is likely to follow the wind curl anomaly (Ekman upwelling) region. The STCC is a surface-trapped feature. This eastward flow arises from the spreading of the thermocline whose deeper

isopycnals slope down toward the poles (westward flow), but shallow isopycnals slope up to the surface (surface eastward flow). Its eddy activity is strongest at the western edge of the domain and weakens on the way to the east. This turbulent zone has been identified as due to baroclinic instability by *Qiu and Chen* [2004]. Within our region, modification of the local wind by the high Marquesas Islands creates a local dipole in the wind curl which generates a countercurrent, the MCC, as has been observed in the lee of other islands.

[46] The use of a regional model embedded in a global model was required by the necessity for high spatial resolution around the steep atolls and islands and in the mesoscale region south of 20° S. For instance, many OGCMs cannot resolve the SECC due to the excessive diffusion [*Furue et al.*, 2007]. Similarly, the simulated STCC mesoscale structure arises through the small-scale, eddy-resolving model dynamics and does not exist in the ECCO-2 MITgcm model.

[47] Seasonal and interannual changes in the currents have major impacts on the Polynesian Islands. *Martinez et al.* [2007] found that current reversals associated with El Niño may have caused ecological perturbations through seaweed invasion in remote archipelagos, and against mean currents. The appearance or displacement of thermal fronts associated with the currents may also have substantial impacts on Tuna behavior [*Zainuddin et al.*, 2006; *Polovina et al.*, 2002]. A follow-up paper will describe the variability of thermal structures and the associated net heat flux budget. The many small-scale effects and recirculation around islands that were found may lead to further investigation.

[48] **Acknowledgments.** The help and stimulating comments of W. Kessler and an anonymous reviewer were greatly appreciated. P. Marchesiello helped to set up the numerical simulation. Insightful comments of the two reviewers greatly helped improve the manuscript. E.M. was supported by a grant from the Research Ministry of French Polynesia. Support from the French Overseas Ministry allowed collaboration with the IRD Noumea LEGOS laboratory. This publication is partially funded by the Joint Institute for the Study of the Atmosphere and Ocean (JISAO) under NOAA Cooperative Agreement NA17RJ1232, contribution 1479, and the Pacific Marine Environmental Laboratory, contribution 3190.

References

- Beckmann, A., and D. B. Haidvogel (1993), Numerical simulation of flow around isolated seamount. part I: Problem formulation and model accuracy, *J. Phys. Oceanogr.*, *23*, 1736–1753, doi:10.1175/1520-0485(1993)023<1736:NSOFAA>2.0.CO;2.
- Boullanger, J. P., J. Rancher, and A. Kartavstev (1993), Etude des trajectoires des bouées dérivantes lancées depuis les atolls de Moruroa et de Fangataufa, *Rapp. SMSR*, *149*, 20 pp.
- Chavanne, C., P. Flament, R. Lumpkin, B. Dousset, and A. Bentamy (2002), Scatterometer observations of wind variations induced by oceanic islands: Implications for wind-driven ocean circulation, *Can. J. Remote Sens.*, *28*, 466–474.
- Chen, S., and B. Qiu (2004), Seasonal variability of the South Equatorial Countercurrent, *J. Geophys. Res.*, *109*, C08003, doi:10.1029/2003JC002243.
- Delcroix, T. (1998), Observed surface oceanic and atmospheric variability in the tropical Pacific at seasonal and ENSO timescales: A tentative overview, *J. Geophys. Res.*, *103*, 18,611–18,634, doi:10.1029/98JC00814.
- Delcroix, T., and J. Picaut (1998), Zonal displacement of the western equatorial Pacific “fresh pool”, *J. Geophys. Res.*, *103*, 1087–1098.
- Delcroix, T., M. J. McPhaden, A. Dessier, and Y. Gouriou (2005), Time and space scales for sea surface salinity in the tropical oceans, *Deep Sea Res., Part 1*, *52*, 787–813, doi:10.1016/j.dsr.2004.11.012.
- Ducet, N., and P. Y. LeTraon (2000), Global high-resolution mapping of ocean circulation from Topex/Poseidon and ERS-1 and -2, *J. Geophys. Res.*, *105*, 19,477–19,498, doi:10.1029/2000JC900063.

- Eldin, G. (1983), Eastward flows of the south equatorial central Pacific, *J. Phys. Oceanogr.*, *13*, 1461–1467, doi:10.1175/1520-0485(1983)013<1461:EFOTSE>2.0.CO;2.
- Fiedler, P. C., and L. D. Talley (2006), Hydrography of the eastern tropical Pacific: A review, *Prog. Oceanogr.*, *69*, 143–180.
- Furue, R., J. P. McCreary, Z. Yu, and D. Wang (2007), Dynamics of the Southern Tsuchiya Jet, *J. Phys. Oceanogr.*, *37*, 531–553, doi:10.1175/JPO3024.1.
- Hanawa, K., and L. D. Talley (2001), *Mode Waters: Ocean Circulation and Climate*, edited by G. Siedler and J. Church, chap. 5.4, pp. 373–386, Academic, San Diego, Calif.
- Huang, R. X., and B. Qiu (1998), The structure of the wind-driven circulation in the subtropical South Pacific, *J. Phys. Oceanogr.*, *28*, 1173–1186, doi:10.1175/1520-0485(1998)028<1173:TSOTWD>2.0.CO;2.
- Ishida, A., H. Mitsudera, Y. Kashino, and T. Kadokura (2005), Equatorial Pacific subsurface countercurrents in a high-resolution global ocean circulation model, *J. Geophys. Res.*, *110*, C07014, doi:10.1029/2003JC002210.
- Jochum, M., and P. Malanotte-Rizzoli (2004), A new theory for the generation of the equatorial subsurface countercurrents, *J. Phys. Oceanogr.*, *34*, 755–771, doi:10.1175/1520-0485(2004)034<0755:ANTFTG>2.0.CO;2.
- Johnson, G. C., and D. W. Moore (1997), The Pacific subsurface countercurrents and an inertial model, *J. Phys. Oceanogr.*, *27*, 2448–2459, doi:10.1175/1520-0485(1997)027<2448:TPSCAA>2.0.CO;2.
- Kessler, W. S. (2006), The circulation of the eastern tropical Pacific: A review, *Prog. Oceanogr.*, *69*, 181–217.
- Kessler, W. S., and L. Gourdeau (2007), The annual cycle of circulation of the southwest subtropical Pacific, analyzed in an Ocean GCM, *J. Phys. Oceanogr.*, *37*, 1610–1627, doi:10.1175/JPO3046.1.
- Kessler, W. S., and M. J. McPhaden (1995), The 1991–1993 El Niño in the central Pacific, *Deep Sea Res., Part II*, *42*, 295–333, doi:10.1016/0967-0645(95)00041-N.
- Kessler, W. S., and B. A. A. Taft (1987), Dynamics heights and zonal geostrophic transports in the central tropical Pacific during 1979–1984, *J. Phys. Oceanogr.*, *17*, 97–122, doi:10.1175/1520-0485(1987)017<0097:DHAZGT>2.0.CO;2.
- Lagerloef, G. S. E., G. T. Mitchum, R. B. Lukas, and P. P. Niiler (1999), Tropical Pacific near-surface currents estimated from altimeter, wind, and drifter data, *J. Geophys. Res.*, *104*, 23,313–23,326, doi:10.1029/1999JC900197.
- Large, W. G., J. C. McWilliams, and S. C. Doneay (1994), Oceanic vertical mixing: A review and a model with a nonlocal boundary layer parameterization, *Rev. Geophys.*, *32*, 363–403, doi:10.1029/94RG01872.
- Laurent, V., K. Maamaatuaiahutapu, J. Maiau, and P. Varney (2004), *Atlas climatologique de la Polynésie française*, 201 pp., Météo France, Tahiti, French Polynesia.
- Lutjeharms, J. R. E., P. Penven, and C. Roy (2003), Modelling the shear edge eddies of the southern Agulhas Current, *Cont. Shelf Res.*, *23*, 1099–1115, doi:10.1016/S0278-4343(03)00106-7.
- Marchesiello, P., J. C. McWilliams, and A. Shchepetkin (2001), Open boundary conditions for long-term integration of regional oceanic models, *Ocean Modell.*, *3*, 1–20, doi:10.1016/S1463-5003(00)00013-5.
- Marchesiello, P., J. C. McWilliams, and A. Shchepetkin (2003), Equilibrium structure and dynamics of the California Current System, *J. Phys. Oceanogr.*, *33*, 753–783, doi:10.1175/1520-0485(2003)33<753:ESADOT>2.0.CO;2.
- Marchesiello, P., S. Herbet, L. Nykjaer, and C. Roy (2004), Eddy-driven dispersion processes in the Canary Current upwelling system: Comparison with the California system, *Globec Int. Newsl.*, *10*, 5–7.
- Martinez, E., K. Maamaatuaiahutapu, C. Payri, and A. Ganachaud (2007), *Turbinaia ornata* invasion in the Tuamotu Archipelago, French Polynesia: Ocean drift connectivity, *Coral Reefs*, *26*, 79–86, doi:10.1007/s00338-006-0160-3.
- McCreary, J. P., Jr., P. Lu, and Z. Yu (2002), Dynamics of the Pacific subsurface countercurrents, *J. Phys. Oceanogr.*, *32*, 2379–2404, doi:10.1175/1520-0485(2002)032<2379:DOTPSC>2.0.CO;2.
- McPhaden, M. J. (1999), Genesis and evolution of the 1997–98 El Niño, *Science*, *283*, 950–954, doi:10.1126/science.283.5404.950.
- Merle, J., H. Rotschi, and B. Voituriez (1969), Zonal circulation in the tropical western South Pacific at 170°E, *Bull. Jpn. Soc. Fish. Oceanogr., Prof. Uda's Comm.*, 91–98.
- Morris, M., D. Roemmich, and B. Cornuelle (1996), Observations of variability in the South Pacific subtropical gyre, *J. Phys. Oceanogr.*, *26*, 2359–2380, doi:10.1175/1520-0485(1996)026<2359:OOVITS>2.0.CO;2.
- Palma, E. D., and R. P. Matano (1998), On the implementation of passive open boundary conditions for a general circulation model: The barotropic mode, *J. Geophys. Res.*, *103*, 1319–1341, doi:10.1029/97JC02721.
- Penven, P. (2003), ROMSTOOLS user's guide, technical report, Inst. de Recherche pour le Dévelop., Paris.
- Penven, P., J. R. E. Lutjeharms, P. Marchesiello, C. Roy, and S. J. Weeks (2001a), Generation of cyclonic eddies by the Agulhas Current in the lee of the Agulhas Bank, *Geophys. Res. Lett.*, *28*, 1055–1058, doi:10.1029/2000GL011760.
- Penven, P., C. Roy, G. B. Brun Drit, A. Colin de Verdière, P. Freon, A. S. Johnson, J. R. E. Lutjeharms, and F. A. Shillington (2001b), A regional hydrodynamic model of upwelling in the Southern Benguela, *S. Afr. J. Sci.*, *97*, 472–475.
- Penven, P., V. Echevin, J. Pasapera, F. Colas, and J. Tam (2005), Average circulation, seasonal cycle, and mesoscale dynamics of the Peru Current System: A modeling approach, *J. Geophys. Res.*, *110*, C10021, doi:10.1029/2005JC002945.
- Picaut, J., M. Ioualalen, T. Delcroix, F. Masia, R. Murtugudde, and J. Vialard (2001), The oceanic zone of convergence on the eastern edge of the Pacific warm pool: A synthesis of results and implications for El Niño Southern Oscillation and biogeochemical phenomena, *J. Geophys. Res.*, *106*, 2363–2386, doi:10.1029/2000JC900141.
- Picaut, J., E. Hackert, A. J. Busalacchi, R. Murtugudde, and G. S. E. Lagerloef (2002), Mechanisms of the 1997–98 El Niño–La Niña, as inferred from space-based observations, *J. Geophys. Res.*, *107*(C5), 3037, doi:10.1029/2001JC000850.
- Polovina, J. J., M. P. Seki, and R. E. Brainard (2002), The role of oceanography in the aggregation and vulnerability of bigeye tuna in the Hawaii longline fishery from satellite, moored, and shipboard time series data: An ongoing study, paper presented at the 15th Meeting of the Standing Committee on Tuna and Billfish, Honolulu, HI.
- Qiu, B., and S. Chen (2004), Seasonal modulations in the eddy field of the South Pacific Ocean, *J. Phys. Oceanogr.*, *34*, 1515–1527, doi:10.1175/1520-0485(2004)034<1515:SMITEF>2.0.CO;2.
- Qiu, B., and T. S. Durland (2002), Interaction between island and the ventilated thermocline: Implications for the Hawaiian Lee Countercurrent, *J. Phys. Oceanogr.*, *32*, 3408–3426, doi:10.1175/1520-0485(2002)032<3408:IBAIAT>2.0.CO;2.
- Rancher, J., and F. Rougerie (1995), L'environnement océanique de l'archipel des Tuamotu (Polynésie française), *Oceanol. Acta*, *18*, 43–60.
- Rancher, J., F. Rougerie, M. Thouard, B. Wauthy, and A. Kartavtseff (1992), *HYDROPOLE: Situations océaniques du Pacifique Central Sud*, 91 pp., SMSR/CEA, Montlhéry, France.
- Reverdin, G., C. Frankignoul, E. Kestenare, and M. J. McPhaden (1994), Seasonal variability in the surface currents of the equatorial Pacific, *J. Geophys. Res.*, *99*, 20,323–20,344.
- Rougerie, F., and J. Rancher (1994), The Polynesian south ocean: Features and circulations, *Mar. Pollut. Bull.*, *29*, 14–25, doi:10.1016/0025-326X(94)90421-9.
- Tomczak, M., and J. S. Godfrey (1994), *Regional Oceanography: An Introduction*, 422 pp., Pergamon, New York.
- Tomczak, M., and M. Herzfeld (1998), Pollutant pathways between Muroa and other Polynesian islands, based on numerical model trajectories, *Mar. Pollut. Bull.*, *36*, 288–297, doi:10.1016/S0025-326X(97)00182-3.
- Tsuchiya, M. (1972), A subsurface north equatorial countercurrent in the Eastern Pacific Ocean: 1. Contribution from Scripps Institution of Oceanography, *J. Geophys. Res.*, *77*, 5981–5986, doi:10.1029/JC077i030p05981.
- Vincent, D. G. (1994), The South Pacific Convergence Zone (SPCZ): A review, *Mon. Weather Rev.*, *122*, 1949–1970, doi:10.1175/1520-0493(1994)122<1949:TSPCZA>2.0.CO;2.
- Wang, B., R. Wu, and R. Lukas (2000), Annual adjustment of the thermocline in the tropical Pacific Ocean, *J. Clim.*, *13*, 596–616, doi:10.1175/1520-0442(2000)013<0596:AAOTTI>2.0.CO;2.
- Wyrtki, K., and B. Kilonsky (1984), Mean water and current structure during the Hawaii-to-Tahiti Shuttle experiment, *J. Phys. Oceanogr.*, *14*(2), 242–254, doi:10.1175/1520-0485(1984)014<0242:MWACSD>2.0.CO;2.
- Xie, S. P., W. T. Liu, Q. Liu, and M. Nonaka (2001), Far-reaching effects of the Hawaiian Islands on the Pacific Ocean–atmosphere system, *Science*, *292*, 2057–2060, doi:10.1126/science.1059781.
- Zainuddin, M., H. Kiyofuji, K. Saitoh, and S. I. Saitoh (2006), Using multi-sensor satellite remote sensing and catch data to detect ocean hot spots for albacore (*Thunnus alalunga*) in the northwestern North Pacific, *Deep Sea Res., Part II*, *53*, 419–431, doi:10.1016/j.dsr2.2006.01.007.

A. Ganachaud and J. Lefevre, Laboratoire d'Etude en Géophysique et Océanographie Spatiales, Institut de Recherche pour le Développement, BP A5, Noumea, New Caledonia.

K. Maamaatuaiahutapu, Laboratoire Terre-Océan, Université de la Polynésie Française, BP 6570, Faaa, 98702, French Polynesia.

E. Martinez, UMR7093, UPMC, CNRS, F-06230 Villefranche-sur-Mer, France. (martinez@obs-vlfr.fr)